



# **Regional flow conditions associated with stratocumulus cloud-eroding boundaries over the southeast Atlantic**

Laura M. Tomkins<sup>\*†</sup>, David B. Mechem

*Department of Geography and Atmospheric Science, University of Kansas, Lawrence, KS.*

Sandra E. Yuter, Spencer R. Rhodes

*Department of Marine, Earth, and Atmospheric Sciences, North Carolina State University,  
Raleigh, NC*

<sup>\*</sup>*Corresponding author:* Laura M. Tomkins, lmtomkin@ncsu.edu

<sup>†</sup>Current affiliation: Center for Geospatial Analytics, North Carolina State University, Raleigh, NC

**Early Online Release:** This preliminary version has been accepted for publication in *Monthly Weather Review*, may be fully cited, and has been assigned DOI 10.1175/MWR-D-20-0250.1. The final typeset copyedited article will replace the EOR at the above DOI when it is published.

## ABSTRACT

Large, abrupt clearing events have been documented in the marine stratocumulus cloud deck over the subtropical Southeast Atlantic Ocean. In these events, clouds are rapidly eroded along a line hundreds–to–thousands of kilometers in length that generally moves westward away from the coast. Because marine stratocumulus clouds exert a strong cooling effect on the planet, any phenomenon that acts to erode large areas of low clouds may be climatically important. Previous satellite-based research suggests that the cloud-eroding boundaries may be caused by westward-propagating atmospheric gravity waves rather than simple advection of the cloud. The behavior of the coastal offshore flow, which is proposed as a fundamental physical mechanism associated with the clearing events, is explored using the Weather Research and Forecasting model. Results are presented from several week-long simulations in the month of May when cloud-eroding boundaries exhibit maximum frequency. Two simulations cover periods containing multiple cloud-eroding boundaries (active periods), and two other simulations cover periods without any cloud-eroding boundaries (null periods). Passive tracers and an analysis of mass flux are used to assess the character of the diurnal west-African coastal circulation. Results indicate that the active periods containing cloud-eroding boundaries regularly experience stronger and deeper nocturnal offshore flow from the continent above the marine boundary layer, compared to the null periods. Additionally, we find that the boundary layer height is higher in the null periods than in the active periods, suggesting that the active periods are associated with areas of thinner clouds that may be more susceptible to cloud erosion.

## 1. Introduction

Stratocumulus clouds are an important component of the climate system. Stratocumulus cover vast areas of the planet and are more abundant than any other type of cloud (Wood 2012). In addition to their large areal coverage, they scatter back to space a large portion of incoming solar radiation, and because the cloud-top temperature is only slightly cooler than the underlying surface, they emit nearly the same amount of infrared radiation as the surface, thus exerting a strong cooling effect on the planet (Hartmann et al. 1992). Large changes to stratocumulus area coverage or optical properties will therefore substantially impact the regional radiation budget. Unfortunately, representing stratocumulus in general circulation models (GCMs) remains an ongoing challenge (Bony and Dufresne 2005; Lin et al. 2014; Wyant et al. 2015).

Dramatic cloud-eroding boundaries have been documented in marine stratocumulus clouds over the southeast Atlantic (SEA) ocean off the western coast of Africa (Yuter et al. 2018). These clearing events arise as long lines ( $>1000$  km) of sharp cloudiness transitions that leave the coast around local midnight and usually propagate westward at a speed of  $\sim 10$  m s<sup>-1</sup>. Large areas of the stratocumulus cloud field rapidly erode along these sharp boundaries (time scale  $<15$  min), leaving behind either clear skies or significantly thinner clouds, which allows increased solar radiation to reach the surface. Since the cloud clearing occurs overnight as well as during the day, no shortwave feedbacks are required. Below the boundary layer inversion, southerly flow associated with the climatologically dominant subtropical high pressure is typically observed over this region during these events. Sequences of satellite images show the cloud-eroding boundaries moving westward while the clouds themselves move northward. This indicates that this cloud-eroding phenomenon is not driven by the southerly flow that exists within the boundary layer and at cloud level.

Yuter et al. (2018) hypothesize that, instead of advection, gravity waves are a likely mechanism for rapidly eroding large areas of cloud over the SEA. Gravity waves have been demonstrated to strongly influence cloud properties over the southeast Pacific (SEP) ocean (O'Dell et al. 2008; Garreaud and Muñoz 2004; Rahn and Garreaud 2010). The gravity waves over the SEA are thought to be excited by an interaction between the offshore flow from the high terrain of coastal Africa and the stratocumulus-topped boundary layer. A hypothetical gravity wave moving through the cloud field would influence cloud properties as follows. For a well-mixed boundary layer, upward wave motion increases the boundary layer depth, thickening the cloud by a proportional amount and increasing the liquid water path (LWP; note that LWP scales as the square of the cloud depth, i.e.,  $LWP \sim h^2$ ). Downward wave motion, on the other hand, reduces the boundary layer depth, resulting in a thinner cloud. Ordinarily, after the wave passes through, the cloud would return to its initial state. In the cloud-eroding cases, however, the cloud is partially or completely cleared. This cloud-eroding phenomenon, therefore, necessitates an irreversible aspect to the gravity-wave mechanism. The speed of the cloud-clearing process and that fact that this type of cloud-clearing often occurs overnight suggests that previous explanations for irreversible cloud transformations based on precipitation or radiative feedbacks (Allen et al. 2013; Connolly et al. 2013) are not primary mechanisms. Synoptic and microphysical influences on cloud clearing (e.g., Kloesel 1992; Crosbie et al. 2016) also act too slowly to explain cloud-clearing occurring in a few 10's of minutes.

Enhanced entrainment is proposed as the particular irreversibility mechanism, whereby gravity-wave passage promotes stronger entrainment, leading to warming and drying within the cloud level at the top of the boundary layer (Yuter et al. 2018). Satellite observations of the cloud boundaries often show high-frequency wave features at the edge of the cloud boundaries, also suggesting that gravity waves may be a factor in the cloud-eroding boundaries. Although the cloud field may not

completely clear, we refer to these transformations as irreversible because over a short period the cloud remains eroded. After clearing, cloud usually reforms after a period between several hours and a day. Rapid cloud clearing may also be aided by the on average thinner clouds over the SEA as compared to the SEP (Zuidema et al. 2016).

The geography of the subtropical western coast of Africa yields a superposition of upslope/downslope flows and sea/land breezes. The coasts of Angola and Namibia feature an escarpment that forms the western edge of a broad region of inland plateau. When the land heats up during the day, a sea breeze is established and onshore and upslope flow prevails. The opposite is true overnight when the land cools down and a land breeze and downslope flow develops. Assuming the cloud-eroding boundaries are related to the strength of the offshore flow, work from Qian et al. (2012) suggests that increasing terrain height may strengthen the overnight offshore flow and increase the potential for gravity waves.

A key characteristic of the cloud-eroding boundaries is that they originate adjacent to the coast near local midnight. Our proposed mechanism for explaining the cloud-eroding boundaries over the SEA involves three distinct components: 1) the nocturnal offshore flow (land breeze and downslope flow) from the continent; 2) the interaction of this offshore flow with the marine boundary layer via the excitation of gravity waves; and 3) a mechanism that renders the cloud field irreversibly modified (cleared) after gravity-wave passage. We use the Weather Research and Forecasting (WRF) model to address aspects of the first two components above by characterizing and comparing the behavior of the coastal circulation for multiple 7-day periods during the month of May that experience cloud-clearing events to periods that do not. The third mechanism is not investigated in this project as it requires a much finer scale model. The simulation methodology and experimental design are described in Section 2. Section 3 discusses the results of the simulations. Section 4 will consider the implications of the results, and Section 5 will present the conclusions of the study.

## 2. Methods

The proposed cloud-eroding hypothesis from Yuter et al. (2018) requires three separate mechanisms: offshore flow, excitation of gravity waves, and a quasi-irreversible clearing mechanism. This research primarily focuses on examining and characterizing the first mechanism, the offshore flow. We provide some insight into the second mechanism in section 4, in particular the excitation gravity-wave undulations in the boundary-layer height field.

### *a. Model Description*

All simulations use the Advanced Research WRF (ARW) model (version 3.9.1), which is based on three-dimensional, nonhydrostatic, compressible dynamics (Skamarock et al. 2008). The Mellor–Yamada–Janjic (MYJ) boundary layer parameterization is employed to represent subgrid-scale vertical transports (Janjic 1994). Horizontal diffusion is parameterized using Smagorinsky first-order closure (Smagorinsky 1963). Microphysical processes are parameterized using the Morrison 2-moment scheme (Morrison et al. 2009). The Kain–Fritsch (KF) scheme is used for the convective parameterization (Kain 2004). It should be noted that deep convection is scarce over our domain during this time of year, except for that associated with the Inter–Tropical Convergence Zone (ITCZ). All simulations employ the NOAH land surface model (Tewari et al. 2004). Longwave radiation is parameterized with the Rapid Radiative Transfer Model (RRTM) scheme, and shortwave radiation is parameterized with the Dudhia scheme (Dudhia 1989; Mlawer et al. 1997). We ran a number of additional simulations with different boundary layer and convective parameterizations to test the sensitivity of the model to parameterization choice. For the boundary layer parameterization, we tested the Yonsei University scheme and the Mellor–Yamada Nakanishi Niino (MYNN) Level–2.5 scheme scheme (Hong et al. 2006; Nakanishi and Niino 2006). For the convective parameterization, we tested the Betts–Miller–Janjic (BMJ) scheme (Janjic 1994).

Simulation results were not particularly sensitive to the choice of boundary layer and/or convective parameterizations.

The domain for the simulations extends from  $\sim 12^{\circ}\text{W}$  to  $\sim 25^{\circ}\text{E}$  in the east-west direction and  $\sim 0^{\circ}\text{N}$  to  $\sim 28^{\circ}\text{S}$  in the north-south direction (Fig. 1). Horizontal grid spacing is 10 km with 430 points in the east-west direction and 298 in the north-south direction (4300 km x 2980 km), with a time step of 40 seconds (Fig. 1). The domain is configured to include a substantial portion of the continent, especially the plateau region, to better resolve the diurnal heating and cooling processes responsible for the land/sea breeze circulation. Because the cloud-eroding boundaries often move as far west as  $4^{\circ}\text{W}$ , the domain also extends well out over the ocean. Initial simulations included a fine (3.33 km), nested domain within the coarse domain; however, the coarse mesh was sufficient in capturing the salient mesoscale features of the coastal circulation. Boundary layer clouds were present in the coarse-domain simulations; however, given the lack of resolution, we were not sufficiently confident in the fidelity of the cloud fields themselves to include them in our analysis. Examining the clouds and entrainment behavior in detail (which we do not do in this project) will require simulations with a finer mesh. The vertical grid has 82 points with variable grid spacing to adequately resolve the boundary layer and inversion structure (supplemental Fig. S1). In the lower 5 km, the grid spacing ranges from 20 m to 400 m, and above that increases up to a maximum of 1000 m (supplemental Fig. S1). The grid spacing near the inversion height is  $\sim 100$  m similar to the regional modeling study of Nelson et al. (2016).

European Centre for Medium-Range Forecasts (ECMWF) interim reanalysis (ERA–Interim; Dee et al. (2011)) data, available every 6 hours (four times daily) with a  $0.75^{\circ}$  latitude/longitude grid spacing, provides initial and boundary conditions for the WRF simulations. Data assimilation update cycles are not employed throughout the simulation, so the ERA–Interim reanalysis influences the WRF simulations only by serving as the initial conditions and via the boundary forcing. Sea

Surface Temperature (SST) data are provided from ERA–Interim reanalysis. Following Nelson et al. (2016), we consider the first 24 hours to be the spin-up period. Due to the coarse resolution of the ERA–Interim data, the initial conditions are very smooth. Over the first day, smaller-scale variability consistent with the WRF grid resolution develop, and by ~24 hours the finer-scale variability in WRF has had a full chance to develop. We consider the model spin-up period to be complete when, visually, fine-scale structures have sufficiently developed. The advantage of using a 10-km WRF simulation over the ERA–Interim reanalysis comes from the increased resolution of the terrain in the WRF simulation, and the finer vertical grid spacing at low levels. The increased resolution improves the numerical representation of elevation differences and likely the ability to simulate finer-scale flows along the coast.

For this analysis, boundary layer heights were calculated by finding gradients in vertical profiles of potential temperature. The lowest height between 200 m and 5000 m that has a potential temperature gradient exceeding 1.5 K / 100 m designates the boundary layer height. We note that regional models and GCMs consistently underestimate boundary layer heights (Wyant et al. 2015; Nelson et al. 2016), so while we do not necessarily trust the absolute boundary layer heights presented in this analysis we do have confidence in the relative boundary layer heights.

### *b. Project Design and Case Selection*

Instead of concentrating on specific clearing events, we performed a series of 7-day simulation periods. All simulation periods take place during May coinciding with the highest frequency of clearing events (Yuter et al. 2018). Of the four, 7-day simulations, two were “active” periods during which most of the days included cloud-eroding boundaries, and two were “null” periods without clearing events. The periods were classified as active or null based on Yuter et al. (2018), who characterized 1911 days over five years as either having cloud-eroding boundaries present (“yes”),

not having boundaries present (“no”), or possibly having boundaries present (“maybe”). Events were characterized using Moderate Resolution Imaging Spectroradiometer (MODIS) corrected reflectance data from the Aqua and Terra satellites (see methods of Yuter et al. (2018) for full details). We chose two periods of both active and null simulations to provide context and increase confidence in the results of each simulation. Table 1 shows the dates spanned by each simulation and whether each day had a clearing event (YES) or not (NO).

### *c. Reanalysis Temperature Comparison*

Accurately representing the nocturnal offshore coastal flow – thought to be a critical component of the cloud-clearing events – requires that WRF capture a diurnal cycle of the 2-m air temperature, as the differences in temperature between the land and ocean drive onshore and offshore pressure gradients. Our region of study has very few in situ observations with which we could validate our model, but as an effort to provide some confidence in our simulations, we compared 2-m temperatures among ERA–Interim (providing the initial and boundary conditions for our simulations), ERA5 (ECMWF Reanalysis 5th Generation; Hersbach and Dee (2016)), and MERRA2 (Modern-Era Retrospective analysis for Research and Applications, Version 2; Gelaro et al. (2017)) with the diurnal cycle from WRF to observe any potential discrepancies in the overnight minimum temperature. In particular, we are interested in differences in overnight minimum temperature among the reanalyses datasets and potential differences between the WRF model and its parent ERA–Interim reanalysis. Broad agreement among these would lend confidence that the WRF simulations are likely to be representing the offshore flow with sufficient fidelity. The diurnal cycle for each dataset is averaged over the red box in Figure 1 and results are presented in Figure 2. The diurnal cycle is similar for all four datasets, yet we note some minor discrepancies. In general, the reanalyses (red, blue, and green lines in Fig. 2) have higher afternoon maximums compared to the

WRF simulations. For the morning minimum temperatures, there is more spread between each dataset. The average minimum temperature for WRF is 287.6 K, 288.9 K for ERA–Interim, 287.6 K for ERA5, and 285.7 K for MERRA2. The WRF minimum temperature is only 1.3 K cooler than the ERA–Interim reanalysis used as the input. The ERA5 is slightly cooler than ERA–Interim, and MERRA2 is a few degrees cooler. In addition to the WRF simulations, both the ERA5 and MERRA2 datasets are output more frequently than the 6-hourly ERA–Interim and may be able to better represent the minimum temperature. This may explain why these datasets have a colder average minimum temperature compared to the ERA–Interim. Regardless, these differences in temperature are not likely to influence our results and provide confidence that the WRF simulations produce similar temperatures compared to other available datasets.

### 3. Results

#### *a. Synoptic overview*

The domain of our simulations lies largely in the subtropics, extending into the tropics and midlatitudes in the northern and southern part of the domain, respectively (Fig. 1). Maps of sea level pressure (SLP) during a representative time in the middle of each simulation at 0000 UTC are shown in Figure 3. Note that the local time over the western portion of the WRF domain is the same as UTC, whereas east of  $7.5^{\circ}\text{E}$ , the local time is UTC+0100. In this study, we consider UTC to be at or near the local time. As is discussed in the sections above, the surface is largely dominated by a semi-permanent high pressure over the ocean due to the descending branch of the Hadley cell circulation and the cool ocean. Additionally, during the austral autumn, high pressure also exists over the land and is often accompanied by a trough of low pressure along the coast, evident in all four simulations (Fig. 3). Although the mean SLP differs slightly across the four

simulations, the SLP pattern differences are minor, suggesting that the clearing events are not tied to specific synoptic-scale features or patterns, a finding which is consistent with the results of Yuter et al. (2018). Additionally, middle- and upper-level fields indicated minimal differences across the four simulations (not shown).

## *b. Offshore flow*

### 1) PASSIVE TRACER FIELDS

In order to explore the behavior of the coastal circulation, we evaluate the evolution of a passive tracer over the simulation domain using the method of Blaylock et al. (2017). A nondimensional scalar tracer field is initialized with a value of unity over a defined volume at the beginning of the simulation. The tracer field is held fixed over that volume for the duration of the simulation, providing a source of the tracer which is then advected away from the region. Two tracer regions are used, one over land and one over the ocean. One tracer region is placed over land near the coast ( $12^{\circ}\text{E}$  to  $15^{\circ}\text{E}$ ,  $15^{\circ}\text{S}$  to  $17^{\circ}\text{S}$ ) where the elevation varies between 200 m and 1500 m to visualize the flow patterns associated with the land-sea breeze circulation. Another tracer region is initialized over the ocean ( $9^{\circ}\text{E}$  to  $11^{\circ}\text{E}$ ,  $15^{\circ}\text{S}$  to  $17^{\circ}\text{S}$ ) to observe the flow patterns within the boundary layer. The tracer field is initialized in the first six vertical levels of the model, up to around 160 m above the surface, covering an area of 22 x 23 grid points (220 km x 230 km). Figure 4 shows plan views and cross sections of the passive tracer fields originating over land at the middle (after first 96 hours) and end (at the last hour) of the first active period. The plan views (Figs. 4a,b) show a quasi-integrated quantity of the tracer field which is calculated by adding up the value of the tracer field in each column. Note that over the source region the vertically summed tracer values can be greater than the initial value of this quantity, as the tracer is transported vertically and is then

replenished in the source region. Animations of both tracer fields for four simulations presented here can be accessed in the supplemental material.

Supplemental animations S1 and S5 show movies of the tracer fields every hour during the first active period. Early in the simulation, the tracer field remains mostly over the continent (Fig. 4a, supplemental animation S1) but as the simulation progresses, the tracer field is evident further out over the ocean (Fig. 4b, supplemental animation S1), eventually reaching as far out as  $0^{\circ}\text{E}$ . Similarly, the tracer field initialized over land in the second active period is advected far out over the ocean over the course of the simulation (Fig. 5b, supplemental animation S2). Vertical cross sections (through  $15.5^{\circ}\text{S}$ , black line in Fig. 4a,b) show the tracer field being lofted up to 3–4 km ( $\sim 1.5\text{--}2.5$  km AGL) over the land during the day when the diurnal heating causes upward motion (Figs. 4a,b, 5a,b, supplemental animations S1, S2). Additionally, the cross sections during the active periods show the tracer field being advected westward above the boundary layer during the overnight hours (Fig. 4d, 5d, supplemental animation S1, S2).

The tracer field initialized over land in the two null periods remains mostly over the continent and is not transported out over the ocean nearly as far as during the active periods (Figs. 6a,b, 7a,b, supplemental animation S3, S4). Similar to the active periods, the tracer field is lofted up over the land during the day associated with the diurnal heating (Figs. 6a,b, 7a,b, supplemental animation S3, S4).

The tracer field initialized in the marine boundary layer is mostly advected to the north and exhibits little east–west dispersion for any period (Figs. 8a,b, 9a,b, 10a,b, 11a,b, supplemental animations S5–8 left panel), consistent with the anticyclonic flow at the surface and within the boundary layer. Because the tracer field stays mostly within the boundary layer, the plan views (Figs. 8a,b, 9a,b, 10a,b, 11a,b, supplemental animations S5–8 left panel; which show a quasi-integrated quantity of the tracer) can be interpreted as boundary layer thickness. Integrated tracer

amount is related to boundary-layer height for two reasons. First, because the tracer concentration in the source region (the lowest 6 grid model grid points, which extends up to 160 m) is held constant, the region constitutes an infinite source. Tracer will be mixed throughout the boundary layer and then replenished over the source region. In this manner, a deeper boundary layer will ultimately have a larger integrated tracer amount than a shallower boundary layer. The second reason for the relationship is related to patterns of divergence and convergence. For example, upward vertical motion and convergence that over time yields a deeper boundary layer produces a mass and tracer flux into the column (see supplemental Fig. S2 for visual explanation).

This relationship between integrated tracer and boundary-layer height can help to identify any perturbations that move through the boundary layer and cause thickening of the boundary layer. Animations of these fields show “ripples” — likely internal gravity waves — that move along the top of the boundary layer in both periods (supplemental animations S5–8). The right panel of the supplemental animations S5–8 show movies of the cross sections shown in Figs. 8c,d, 9c,d, 10c,d, and 11c,d and also show these waves in the boundary layer height (seen both in the tracer fields themselves and in the calculated boundary layer height). The idea of darker shading being proportional to a deeper boundary layer also helps to compare the boundary layer height between the two periods. The plan views of the marine tracer field in the active periods are lighter than the tracer fields in the null periods, which indicates that the boundary layer in the null periods is deeper overall than the boundary layer in the active periods (Figs. 8a,b, 9a,b, 10a,b, 11a,b, supplemental animations S5–8 left panel). The deeper boundary layer is additionally confirmed in the cross sections (Figs. 8c,d, 9c,d, 10c,d, 11c,d, supplemental animations S5–8 right panel) which show the calculated marine boundary layer height as a dashed line. The differences in boundary layer height are discussed more in the following sections.

## 2) MASS FLUX

To better understand the offshore flow in this region, we analyzed the zonal mass flux over the latitudes annotated by the 200-km wide black line in Figure 1. For each grid column along the black line, we calculated the profiles of mass flux by multiplying the  $u$  component of the wind by the air density and then averaged the profiles. Figure 12 shows a time series of these mass flux profiles over the lowest 2 km for each simulation. Negative values (purple colors) indicate areas where the flow has an offshore component and positive values (green colors) indicate areas where the flow has an onshore component. The patterns in each period are consistent with a typical land-sea breeze circulation with offshore flow overnight (land breeze) and onshore flow during the day (sea breeze). The areas of overnight offshore flow in the active periods are stronger and deeper (extending all the way up to 2 km at times) compared to the overnight offshore flow in the null periods (Fig. 12). Additionally, the null periods typically have stronger onshore flow between 500–1000 m compared to the active periods. The average boundary layer height is visualized by the dashed black line in each image. The overnight offshore flow generally remains above the boundary layer, with the exception of the second active period where the offshore flow intrudes into the boundary layer (Fig. 12c).

It is possible that the strengthened overnight offshore flow may be explained by cooler temperatures over the highlands; however, this is not the case. We calculated the 00 (midnight local time) UTC temperature averaged over the red box in Figure 1 and compared it to the average mass flux between 0200–0500 UTC and 0500–0800 UTC at 50 m and 100 m above the average boundary layer height. We found that there is no substantial correlation between the overnight temperature and the offshore mass flux (Fig. 13).

Theoretically, we should also expect to see a stronger difference in pressure and temperature in active periods with stronger offshore flow, but this is also not the case. We calculated the difference between the 0000 UTC 2 m temperature over land (red box in Figure 1) and ocean (similar extent off the coast; 15–20 °S, 5–10 °E) and compared it to the average mass flux between 0200–0500 UTC. We did the same for the surface pressure over land and over the ocean. We did not find any clear patterns that would indicate a stronger temperature or pressure difference would yield a stronger mass flux (Fig. 14). We likely do not see any relationship here because the stable layer over the ocean complicates the flow. When the flow moves offshore, it rides over the marine stable layer, so it is likely that the 2-m temperature and surface pressure over the ocean are not relevant to the strength of the offshore flow in this case.

### *c. Boundary Layer Height*

In order to observe the east-west differences in the boundary layer height between the active and null periods, we calculated the median boundary layer height over 15°S to 20°S and between 0° and 12°E for an overnight period (0200–0600 UTC) for both the active and null periods (Fig. 15). All periods have a low boundary layer height near the coast (~100–200 m) and then increasing with height toward the west which is also consistent with the climatological patterns in boundary layer height for this region. Additionally, the patterns in boundary layer height confirm the idea presented in the previous sections that the boundary layer height is lower in the active periods than it is in the null periods. It is important to note that since boundary layer heights are often underestimated in models (Wyant et al. 2015), the absolute height differences here are not as important as the relative height differences between the two periods.

We calculated time series of vertical motion,  $w$  [ $\text{cm s}^{-1}$ ], similar to figure 12 and taken along the line indicated in Fig. 1, to discern any difference in large-scale vertical motion between the active

and null periods. We found that the active periods have stronger subsidence than the null periods (Fig. 16), which may help explain why the active periods have shallower boundary layers than the null periods. At 1500 m, the average vertical motion for the active 1 period was  $-0.22 \text{ cm s}^{-1}$ ,  $-0.28 \text{ cm s}^{-1}$  for the active 2 period,  $-0.19 \text{ cm s}^{-1}$  for the null 1 period, and  $-0.18 \text{ cm s}^{-1}$  for the null 2 period.

#### 4. Discussion

The passive tracer fields and mass flux calculations both indicate that the active periods are characterized by strong overnight offshore flow and weak afternoon onshore flow. The opposite is true for the null periods, when the overnight offshore flow is weak and the afternoon onshore flow is strong. Passive tracers suggest that the offshore flow from the continent during the active period overrides the marine boundary layer and can extend out as far as  $9^\circ\text{E}$  for any given day as compared to  $12^\circ\text{E}$  for null periods. Additionally, the strong afternoon onshore flow in the null periods would act to suppress both westward advection and gravity-wave propagation. All else being equal, a shallower boundary layer has thinner stratocumulus clouds than a deeper boundary layer (Wood 2012). Because the active period has a shallower boundary layer than the null period, we infer the active period clouds are more susceptible to any erosion mechanism compared to the null period.

Birch and Reeder (2013) proposed that the interaction of the offshore flow in northwest Australia with the marine boundary layer triggered gravity waves responsible for wave cloud events in the region. Since the terrain of the Australian coast slopes downward from about 300 m ASL, terrain plays only a minimal role in driving a downslope component of the flow. For this reason, the flow off the continent largely acts as an idealized land-breeze circulation, with the horizontal offshore flow interacting with the marine boundary layer. In contrast to the northwest Australian coast, the substantial coastal escarpment (maximum altitude 1300 m) along the African coast yields a strong

downslope component of the flow in addition to the land-breeze, which greatly complicates the interaction between the offshore flow and the marine boundary layer.

We propose a conceptual model for interaction between the off-shore flow and marine boundary layer that includes interactions along both the eastern edge and top edge of the marine boundary layer (Fig. 17). Even though the downslope flows are driven by nocturnal cooling, adiabatic warming ensures that the offshore flow remains warmer than the marine boundary layer, leading to the offshore flow largely overrunning the marine boundary layer. This conceptual model includes the potential gravity wave trigger of a downward impulse from the offshore flow interacting with the top of the marine boundary layer. Additionally, the offshore flow moving above the marine boundary layer would enhance the shear across the boundary layer top, which would promote enhanced entrainment (i.e. mixing of warm, dry, free-tropospheric air into the boundary layer), acting to erode the cloud. The details of how the gravity wave and shear would interact remain an area of future research.

## 5. Conclusions

In this study, we examine the physical mechanisms associated with stratocumulus cloud-eroding boundaries over the southeast Atlantic. We use the WRF model to run simulations over two multi-day periods when several days of cloud-eroding boundaries occur (active periods), and two periods without cloud-eroding boundaries (null periods). We focus on analyzing the overnight offshore flow using SLP maps, passive tracer fields, and mass flux calculations. Our analysis emphasizes the roles of the offshore flow and boundary layer depth. Our main conclusions are as follows:

- Active periods with cloud-eroding boundaries have stronger overnight offshore flow than null periods without clearing events. We propose that the stronger offshore flow likely contributes

to two mechanisms relevant to cloud-eroding boundaries—triggering gravity waves and increasing shear at the top of the marine boundary layer.

- Active periods have lower boundary-layer heights than null periods. A lower marine boundary layer top is easier for an offshore flow of a given temperature and mass flux to override. Additionally, lower boundary-layer heights are associated with thinner clouds, which may cause the clouds in the active period to be more susceptible to erosion.
- The dominant overnight offshore and afternoon onshore flows that delineate active from null periods are not explained by temperature differences over land. This non-correlation suggests that there are other factors which contribute to the strength of the offshore flow other than the cooling over land.

Our analysis was not able to separate the temporal and spatial scales between the synoptic and diurnal. The assumption of a diurnal cycle superimposed over a quasi-steady, barotropic background is plainly an oversimplification. The background synoptic state is highly varying on multi-day timescales, as demonstrated by de Szoeke et al. (2016). This reality makes teasing the two scales apart — and unambiguously identifying the conditions conducive to cloud-eroding boundaries — highly difficult. As part of disentangling the synoptic and diurnal contributions to the variability, future analysis should examine the role of the ageostrophic flow during these periods. Specifically, a more thorough momentum budget analysis should be completed to better separate the different mechanisms presented in this work.

Work by Patricola and Chang (2017) suggests that the shape of the African coastline and resulting localized convergence and divergence patterns have implications on the coastal jet in this region. Further analysis should examine the associations of the coastal jet as a function of synoptic patterns in determining days with or without clearing events.

A key missing piece to resolving the physical mechanisms responsible for cloud-eroding boundaries are the detailed physics occurring within the low cloud deck at convective scales before, during, and after gravity wave passage. A field experiment centered on the southeast Atlantic including soundings, lidar, cloud radar, and in situ data sets that transect cloud-eroding boundaries would advance knowledge and address several key questions.

*Data availability statement.* WRF configuration files used to conduct the simulations, and processed datasets for some of the figures are available at DOI 10.17605/OSF.IO/X7F5C. The ERA–Interim product can be downloaded from The NCAR Research Data Archive. For the full time-dependent 3D WRF simulation output, please contact the corresponding author (lmtomkin@ncsu.edu).

*Acknowledgments.* The authors greatly appreciate advice and feedback from David Rahn, Matthew Miller, and Lucas McMichael. The authors also wish to thank three anonymous reviewers for their comments and suggestions for improving this manuscript. This work was supported by NSF AGS grants 1656237 and 1656314 and U.S. Department of Energy grant DE–SC0016522.

## References

- Allen, G., and Coauthors, 2013: Gravity-wave-induced perturbations in marine stratocumulus. *Quart. J. Roy. Meteor. Soc.*, **139** (670), 32–45, doi:10.1002/qj.1952.
- Birch, C. E., and M. J. Reeder, 2013: Wave-cloud lines over northwest Australia. *Quart. J. Roy. Meteor. Soc.*, **139** (674), 1311–1326, doi:10.1002/qj.2043.
- Blaylock, B. K., J. D. Horel, and E. T. Crosman, 2017: Impact of Lake Breezes on Summer Ozone Concentrations in the Salt Lake Valley. *J. Appl. Meteor. Climatol.*, **56** (2), 353–370, doi:10.1175/Jamc-D-16-0216.1.

- Bony, S., and J. L. Dufresne, 2005: Marine boundary layer clouds at the heart of tropical cloud feedback uncertainties in climate models. *Geophys. Res. Lett.*, **32** (20), doi:10.1029/2005gl023851.
- Connolly, P. J., G. Vaughan, P. Cook, G. Allen, H. Coe, T. W. Choullarton, C. Dearden, and A. Hill, 2013: Modelling the effects of gravity waves on stratocumulus clouds observed during VOCALS-UK. *Atmos. Chem. Phys.*, **13** (14), 7133–7152, doi:10.5194/acp-13-7133-2013.
- Crosbie, E., and Coauthors, 2016: Stratocumulus Cloud Clearings and Notable Thermodynamic and Aerosol Contrasts across the Clear-Cloudy Interface. *Journal of the Atmospheric Sciences*, **73** (3), 1083–1099, doi:10.1175/Jas-D-15-0137.1.
- de Szoeke, S. P., K. L. Verlinden, S. E. Yuter, and D. B. Mechem, 2016: The Time Scales of Variability of Marine Low Clouds. *J. Climate*, **29** (18), 6463–6481, doi:10.1175/Jcli-D-15-0460.1.
- Dee, D. P., and Coauthors, 2011: The ERA-Interim reanalysis: configuration and performance of the data assimilation system. *Quart. J. Roy. Meteor. Soc.*, **137** (656), 553–597, doi:10.1002/qj.828.
- Dudhia, J., 1989: Numerical Study of Convection Observed during the Winter Monsoon Experiment Using a Mesoscale Two-Dimensional Model. *Journal of the Atmospheric Sciences*, **46** (20), 3077–3107, doi:10.1175/1520-0469(1989)046<3077:Nsocod>2.0.Co;2.
- Garreaud, R. D., and R. Muñoz, 2004: The diurnal cycle in circulation and cloudiness over the subtropical southeast Pacific: A modeling study. *J. Climate*, **17** (8), 1699–1710, doi:10.1175/1520-0442(2004)017<1699:Tdcica>2.0.Co;2.
- Gelaro, R., and Coauthors, 2017: The Modern-Era Retrospective Analysis for Research and Applications, Version 2 (MERRA-2). *J. Climate*, **30** (14), 5419–5454, doi:10.1175/Jcli-D-16-0758.1.

- Hartmann, D. L., M. E. Ockertbell, and M. L. Michelsen, 1992: The Effect of Cloud Type on Earths Energy-Balance - Global Analysis. *J. Climate*, **5** (11), 1281–1304, doi:10.1175/1520-0442(1992)005<1281:Teocto>2.0.Co;2.
- Hersbach, H., and D. Dee, 2016: ERA-5 reanalysis is in production. *ECMWF newsletter*, 7.
- Hong, S. Y., Y. Noh, and J. Dudhia, 2006: A new vertical diffusion package with an explicit treatment of entrainment processes. *Mon. Wea. Rev.*, **134** (9), 2318–2341, doi:10.1175/Mwr3199.1, URL ://WOS:000240654000002.
- Janjic, Z. I., 1994: The Step-Mountain Eta Coordinate Model - Further Developments of the Convection, Viscous Sublayer, and Turbulence Closure Schemes. *Mon. Wea. Rev.*, **122** (5), 927–945, doi:10.1175/1520-0493(1994)122<0927:Tsmecm>2.0.Co;2.
- Kain, J. S., 2004: The Kain-Fritsch convective parameterization: An update. *J. Appl. Meteor.*, **43** (1), 170–181, doi:10.1175/1520-0450(2004)043<0170:Tkcpau>2.0.Co;2.
- Kloesel, K. A., 1992: Marine Stratocumulus Cloud Clearing Episodes Observed during Fire. *Mon. Wea. Rev.*, **120** (4), 565–578, doi:10.1175/1520-0493(1992)120<0565:Msceco>2.0.Co;2.
- Lin, J.-L., T. Qian, and T. Shinoda, 2014: Stratocumulus clouds in southeastern pacific simulated by eight cmip5–cfmip global climate models. *JCLI*, **27** (8), 3000–3022.
- Mlawer, E. J., S. J. Taubman, P. D. Brown, M. J. Iacono, and S. A. Clough, 1997: Radiative transfer for inhomogeneous atmospheres: RRTM, a validated correlated-k model for the longwave. *Journal of Geophysical Research-Atmospheres*, **102** (D14), 16 663–16 682, doi:10.1029/97jd00237.
- Morrison, H., G. Thompson, and V. Tatarskii, 2009: Impact of Cloud Microphysics on the Development of Trailing Stratiform Precipitation in a Simulated Squall Line: Comparison of One- and Two-Moment Schemes. *Mon. Wea. Rev.*, **137** (3), 991–1007, doi:10.1175/2008mwr2556.1.

- Nakanishi, M., and H. Niino, 2006: An improved Mellor-Yamada level-3 model: Its numerical stability and application to a regional prediction of advection fog. *Boundary-Layer Meteorology*, **119** (2), 397–407, doi:10.1007/s10546-005-9030-8.
- Nelson, K. J., D. B. Mechem, and Y. L. Kogan, 2016: Evaluation of Warm-Rain Microphysical Parameterizations in Mesoscale Simulations of the Cloudy Marine Boundary Layer. *Mon. Wea. Rev.*, **144** (6), 2137–2154, doi:10.1175/Mwr-D-15-0266.1.
- O’Dell, C. W., F. J. Wentz, and R. Bennartz, 2008: Cloud liquid water path from satellite-based passive microwave observations: A new climatology over the global oceans. *J. Climate*, **21** (8), 1721–1739, doi:10.1175/2007jcli1958.1.
- Patricola, C. M., and P. Chang, 2017: Structure and dynamics of the benguela low-level coastal jet. *Climate Dynamics*, **49** (7-8), 2765–2788.
- Qian, T., C. C. Epifanio, and F. Zhang, 2012: Topographic effects on the tropical land and sea breeze. *JAS*, **69** (1), 130–149.
- Rahn, D. A., and R. Garreaud, 2010: Marine boundary layer over the subtropical southeast Pacific during VOCALS-REx - Part 1: Mean structure and diurnal cycle. *Atmos. Chem. Phys.*, **10** (10), 4491–4506, doi:10.5194/acp-10-4491-2010.
- Skamarock, W. C., and Coauthors, 2008: A Description of the Advanced Research WRF Version 3. *NCAR Tech. Note NCAR/TN-475+STR*, 113, doi:10.5065/D68S4MVH.
- Smagorinsky, J., 1963: General circulation experiments with the primitive equations: I. The basic experiment. *Mon. Wea. Rev.*, **91** (3), 99–164.

- Tewari, M., and Coauthors, 2004: Implementation and verification of the unified NOAA land surface model in the WRF model. *20th conf. on weather analysis and forecasting/16th conf. on numerical weather prediction*, Vol. 1115, 2165–2170.
- Wood, R., 2012: Stratocumulus Clouds. *Mon. Wea. Rev.*, **140** (8), 2373–2423, doi:10.1175/Mwr-D-11-00121.1.
- Wyant, M. C., and Coauthors, 2015: Global and regional modeling of clouds and aerosols in the marine boundary layer during VOCALS: the VOCA intercomparison. *Atmos. Chem. Phys.*, **15** (1), 153–172, doi:10.5194/acp-15-153-2015.
- Yuter, S. E., J. D. Hader, M. A. Miller, and D. B. Mechem, 2018: Abrupt cloud clearing of marine stratocumulus in the subtropical southeast Atlantic. *Science*, doi:10.1126/science.aar5836.
- Zuidema, P., and Coauthors, 2016: Challenges and Prospects for Reducing Coupled Climate Model SST Biases in the Eastern Tropical Atlantic and Pacific Oceans: The U.S. CLIVAR Eastern Tropical Oceans Synthesis Working Group. *Bull. Amer. Meteor. Soc.*, **97** (12), 2305–+, doi:10.1175/Bams-D-15-00274.1.

## LIST OF TABLES

**Table 1.** Dates and clearing event characteristic (“yes”, “no”, “maybe”; see text for full description) of each simulation. Italicized dates indicate those not analyzed to account for spin-up. . . . . 25

TABLE 1. Dates and clearing event characteristic (“yes”, “no”, “maybe”; see text for full description) of each simulation. *Italicized dates indicate those not analyzed to account for spin-up.*

Active #1		Active #2		Null #1		Null #2	
<i>20 May 2013</i>	YES	<i>22 May 2014</i>	NO	<i>21 May 2008</i>	NO	<i>01 May 2009</i>	NO
21 May 2013	NO	23 May 2014	YES	22 May 2008	NO	02 May 2009	NO
22 May 2013	YES	24 May 2014	YES	23 May 2008	NO	03 May 2009	NO
23 May 2013	NO	25 May 2014	YES	24 May 2008	NO	04 May 2009	NO
24 May 2013	YES	26 May 2014	YES	25 May 2008	NO	05 May 2009	NO
25 May 2013	YES	27 May 2014	YES	26 May 2008	NO	06 May 2009	NO
26 May 2013	YES	28 May 2014	YES	27 May 2008	NO	07 May 2009	NO

## LIST OF FIGURES

<b>Fig. 1.</b>	WRF domain configuration for the simulations with terrain (m; contoured every 50 m). Mesh D01 (black box) has horizontal grid spacing of 10 km. Fine mesh simulations with grid spacing 3.33 km have been performed but are not included in this report or on this figure. Red box indicates location of temperature analysis, black line indicates locations of mass flux calculations completed later in the analysis. . . . .	28
<b>Fig. 2.</b>	2-m temperatures diurnal cycle for WRF (bold black line), ERA–Interim (red line), ERA5 (blue line), and MERRA2 (green line) data valid for 20 May 2013 0000 UTC to 27 May 2013 0000 UTC averaged over 15–20°S, 15–20°E. . . . .	29
<b>Fig. 3.</b>	Simulated sea-level pressure (hPa; contoured every 1 hPa) and 10-m winds (key in upper right) for a representative time in the middle of the (a) Active # 1 (24 May 2013 0000 UTC), (b) Null # 1 (25 May 2008 0000 UTC), (c) Active #2 (26 May 2014 0000 UTC), and (d) Null # 2 (5 May 2009 0000 UTC) simulations. . . . .	30
<b>Fig. 4.</b>	(a)–(b) Plan views of the simulated column-integrated ‘land’ passive tracer field (red shaded, dimensionless) for two times during the active # 1 period (24 May 2013 0000 UTC and 27 May 2013 0000 UTC). (c)–(d) Vertical cross section of tracer along ~15.5°S line indicated in (a) and (b) and boundary layer height (dashed black line). Note that the cross section is not exactly along 15.5 °S because the WRF domain does not follow a constant-latitude circle. . . . .	31
<b>Fig. 5.</b>	As in Fig. 4 but for two times during the active #2 period (26 May 2014 0000 UTC and 29 May 2014 0000 UTC). . . . .	32
<b>Fig. 6.</b>	As in Fig. 4 but for two times during the null #1 period (25 May 2008 0000 UTC and 28 May 2008 0000 UTC). . . . .	33
<b>Fig. 7.</b>	As in Fig. 4 but for two times during the null #2 period (5 May 2009 0000 UTC and 8 May 2009 0000 UTC). . . . .	34
<b>Fig. 8.</b>	(a)–(b) Plan views of the simulated column-integrated ‘ocean’ passive tracer field (blue shaded, dimensionless) for the same two active # 1 period times as in Fig. 4. (c)–(d) Vertical cross section of tracer along 15.5°S line indicated in (a) and (b) and boundary layer height (dashed black line). . . . .	35
<b>Fig. 9.</b>	As in Fig. 8 but for the same two active #2 period times as in Fig. 5. . . . .	36
<b>Fig. 10.</b>	As in Fig. 8 but for the same two null #1 period times as in Fig. 6. . . . .	37
<b>Fig. 11.</b>	As in Fig. 8 but for the same two null #2 period times as in Fig. 7. . . . .	38
<b>Fig. 12.</b>	Time series of mass flux ( $\text{kg m}^{-2} \text{s}^{-1}$ ) from 0 m to 2000 m every 50 m for (a) Active # 1 period, (b) Null # 1 period, (c) Active #2 period, and (d) Null #2 period, averaged over the 200-km wide black line in Figure 1. Dashed black line shows averaged boundary layer height. Purple colors indicate areas where there is offshore flow and green colors indicate areas where there is onshore flow. . . . .	39
<b>Fig. 13.</b>	Scatter plot of 0000 UTC temperature averaged over red box in Figure 1 compared to 0200–0500 UTC (left) and 0500–0800 UTC (right) average mass flux from black line in Figure 1. Points are distinguished for each simulation, Active #1 (dark blue), Active #2 (light blue),	

	Null #1 (dark green), and Null #2 (light green) and for 50 m (circles) and 100 m (squares) above the average boundary layer height. . . . .	40
<b>Fig. 14.</b>	As in Fig. 13 except for the difference between 2 m temperature over land and ocean (left) and difference between surface pressure over land and ocean compared to the 0200–0500 UTC average mass flux. Ocean values are averaged over 15–20 °S and 5–10 °E. . . . .	41
<b>Fig. 15.</b>	Calculated median boundary layer height (m) as a function of longitude calculated over a latitude range from 15°S to 20°S for the Active #1 period (dark blue), Active #2 period (light blue), Null #1 period (dark green) and Null #2 period (light green) during the night (0200–0600 UTC). Shaded regions show the interquartile range. . . . .	42
<b>Fig. 16.</b>	As in Fig. 12 except for vertical motion ( $\text{cm s}^{-1}$ ). Light green and yellow colors indicate areas of downward motion and dark blue colors indicate areas of upward or negligible motion. . . . .	43
<b>Fig. 17.</b>	Conceptual model showing cross sections for 3 sequential times (a–c) during a cloud-eroding event. The cross sections are along a representative latitude (e.g. 15.5°S as in Figs. 4–11) and indicate the relative locations of the MBL top (black line) and land (brown). Gray arrows represent the offshore flow from the continent. Blue dashed line at 12°E in (b) and (c) indicate the original position of the MBL edge in (a). The red arrow in (b) shows the motion of the gravity wave. The green box in (c) indicates a region of shear instability generated by the offshore flow overriding the MBL. . . . .	44

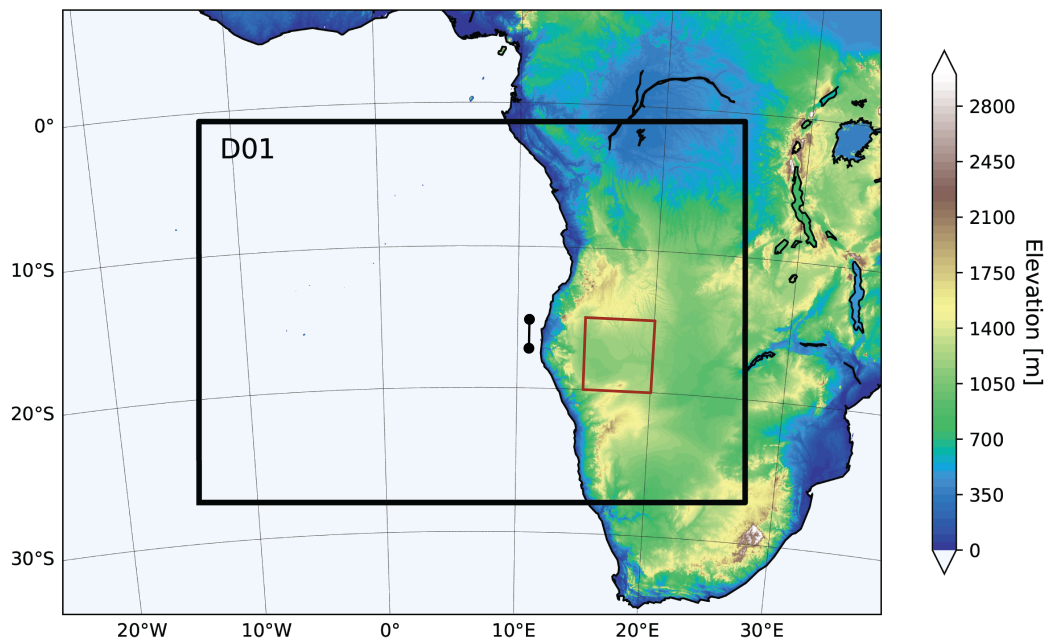


FIG. 1. WRF domain configuration for the simulations with terrain (m; contoured every 50 m). Mesh D01 (black box) has horizontal grid spacing of 10 km. Fine mesh simulations with grid spacing 3.33 km have been performed but are not included in this report or on this figure. Red box indicates location of temperature analysis, black line indicates locations of mass flux calculations completed later in the analysis.

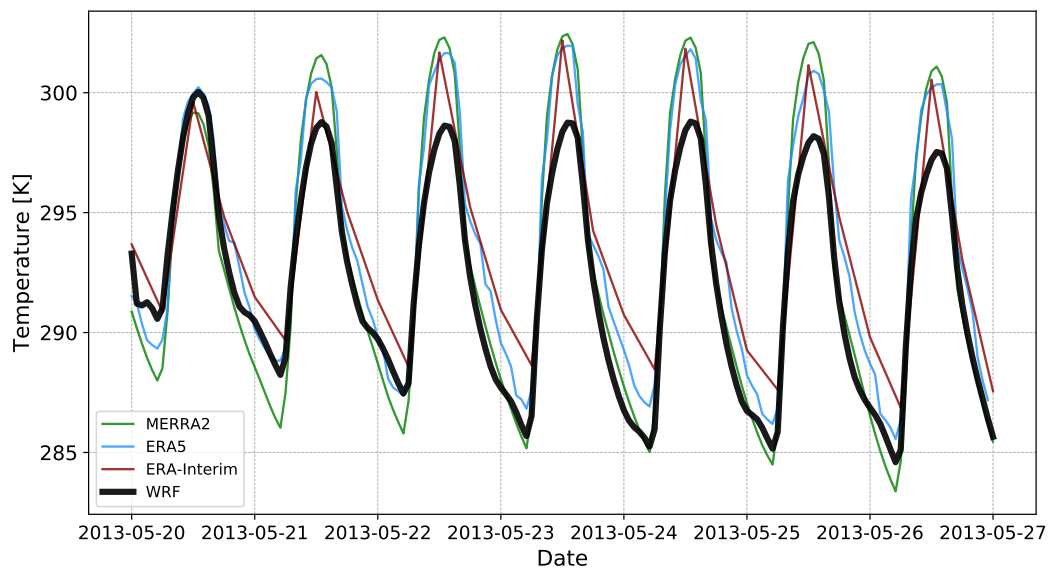


FIG. 2. 2-m temperatures diurnal cycle for WRF (bold black line), ERA-Interim (red line), ERA5 (blue line), and MERRA2 (green line) data valid for 20 May 2013 0000 UTC to 27 May 2013 0000 UTC averaged over 15–20°S, 15–20°E.

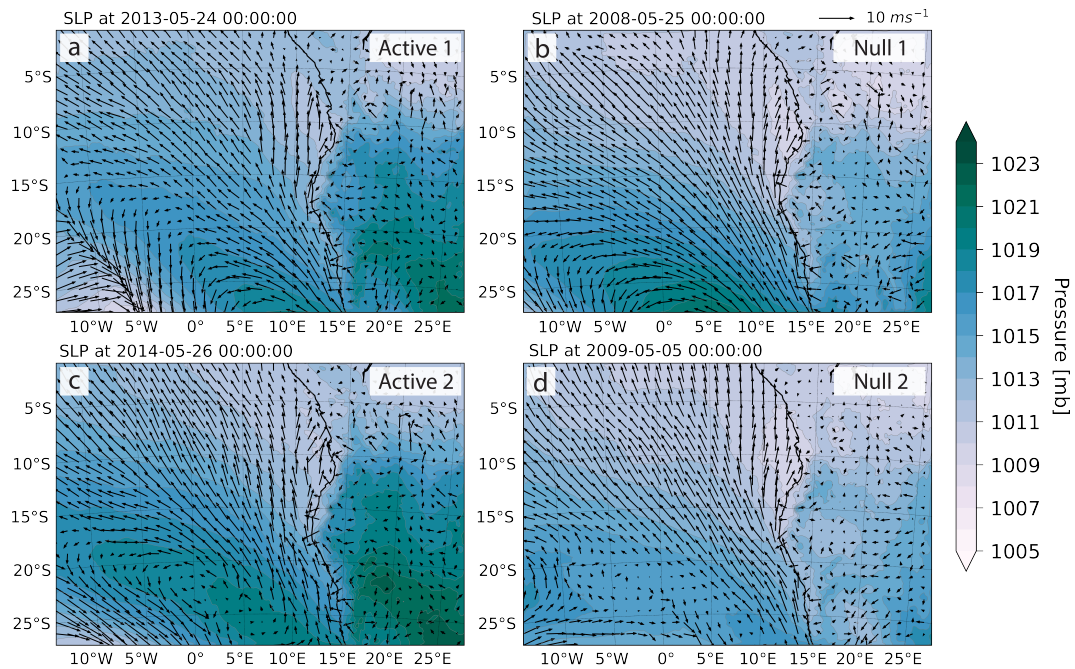


FIG. 3. Simulated sea-level pressure (hPa; contoured every 1 hPa) and 10-m winds (key in upper right) for a representative time in the middle of the (a) Active # 1 (24 May 2013 0000 UTC), (b) Null # 1 (25 May 2008 0000 UTC), (c) Active # 2 (26 May 2014 0000 UTC), and (d) Null # 2 (5 May 2009 0000 UTC) simulations.

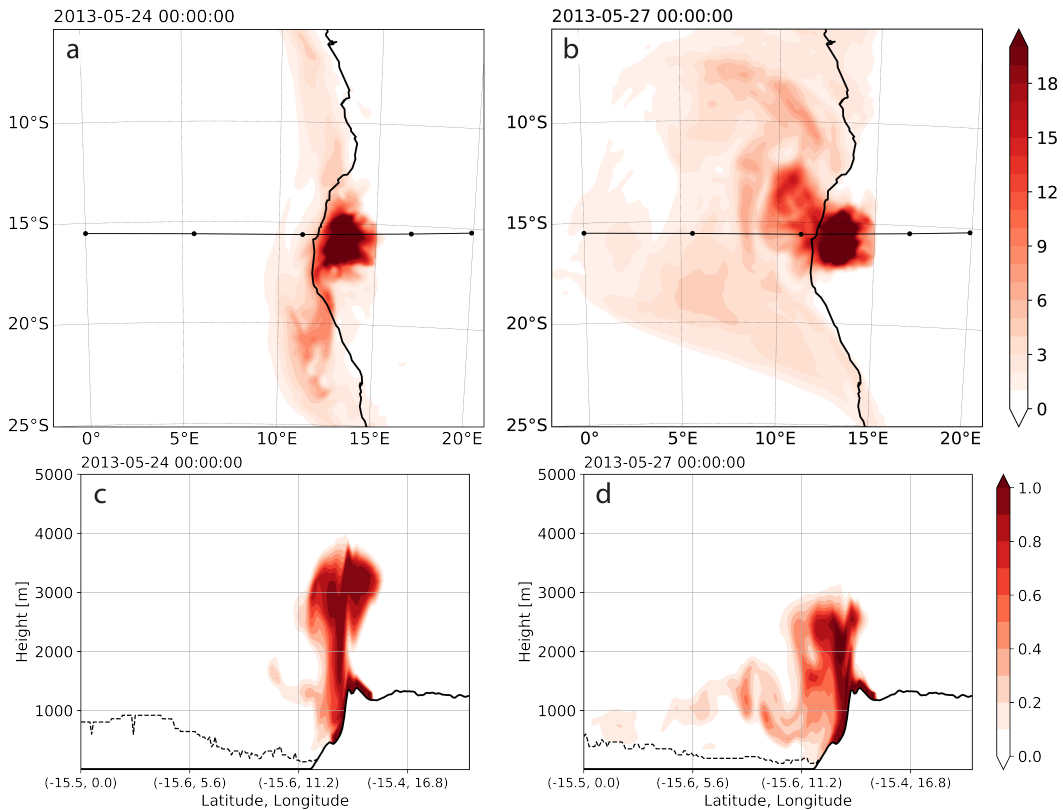


FIG. 4. (a)–(b) Plan views of the simulated column-integrated ‘land’ passive tracer field (red shaded, dimensionless) for two times during the active # 1 period (24 May 2013 0000 UTC and 27 May 2013 0000 UTC). (c)–(d) Vertical cross section of tracer along  $\sim 15.5^\circ\text{S}$  line indicated in (a) and (b) and boundary layer height (dashed black line). Note that the cross section is not exactly along  $15.5^\circ\text{S}$  because the WRF domain does not follow a constant-latitude circle.

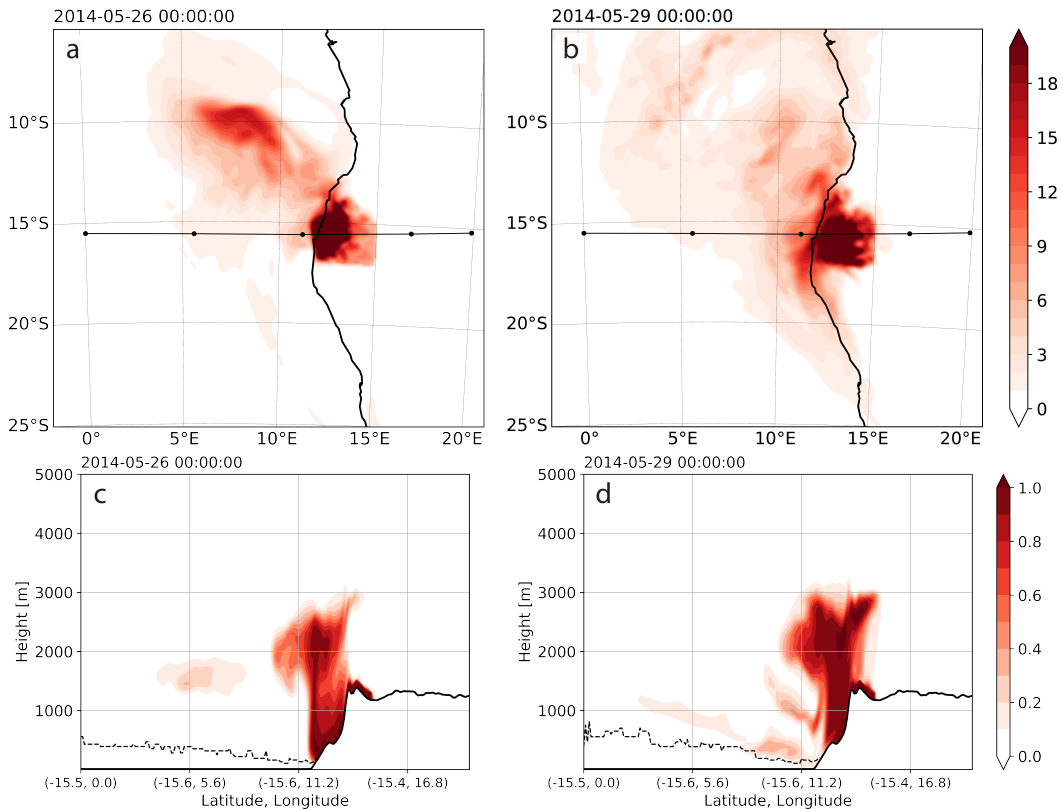


FIG. 5. As in Fig. 4 but for two times during the active #2 period (26 May 2014 0000 UTC and 29 May 2014 0000 UTC).

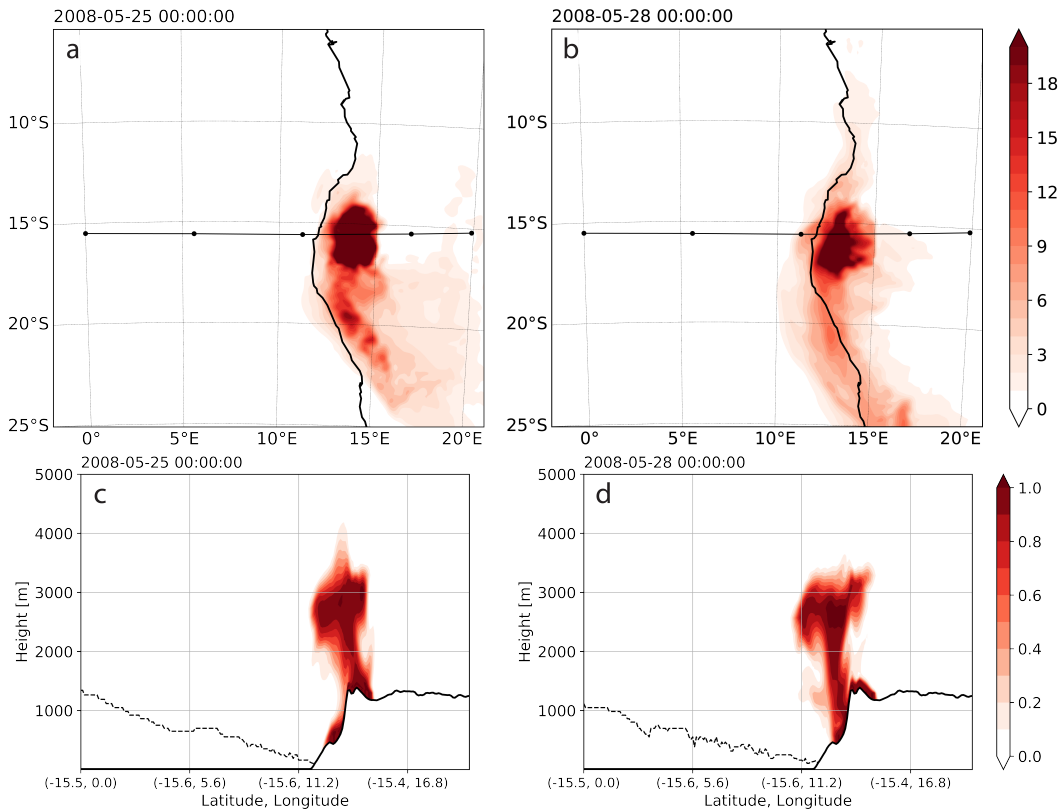


FIG. 6. As in Fig. 4 but for two times during the null #1 period (25 May 2008 0000 UTC and 28 May 2008 0000 UTC).

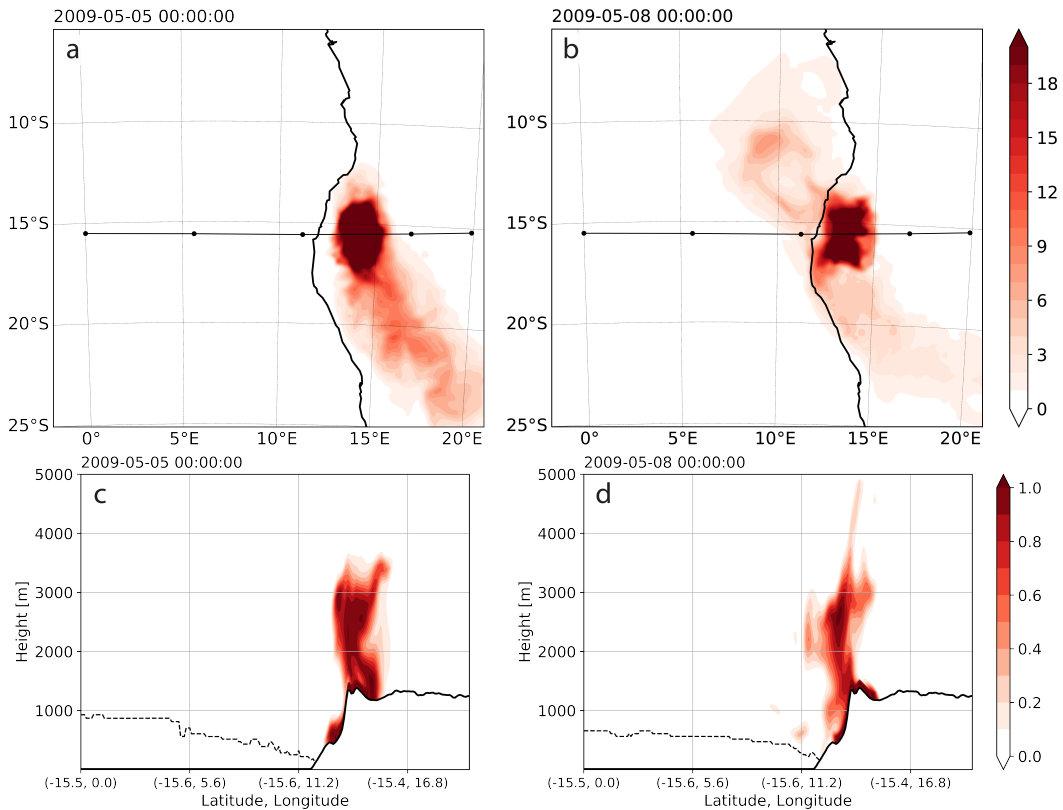


FIG. 7. As in Fig. 4 but for two times during the null #2 period (5 May 2009 0000 UTC and 8 May 2009 0000 UTC).

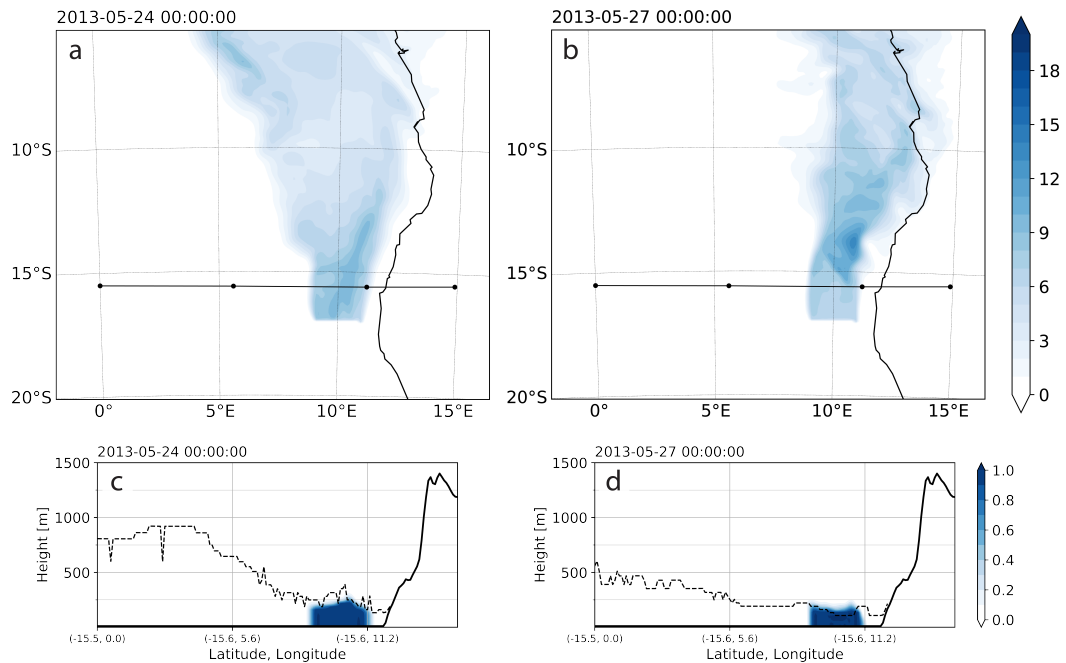


FIG. 8. (a)–(b) Plan views of the simulated column-integrated ‘ocean’ passive tracer field (blue shaded, dimensionless) for the same two active # 1 period times as in Fig. 4. (c)–(d) Vertical cross section of tracer along 15.5°S line indicated in (a) and (b) and boundary layer height (dashed black line).

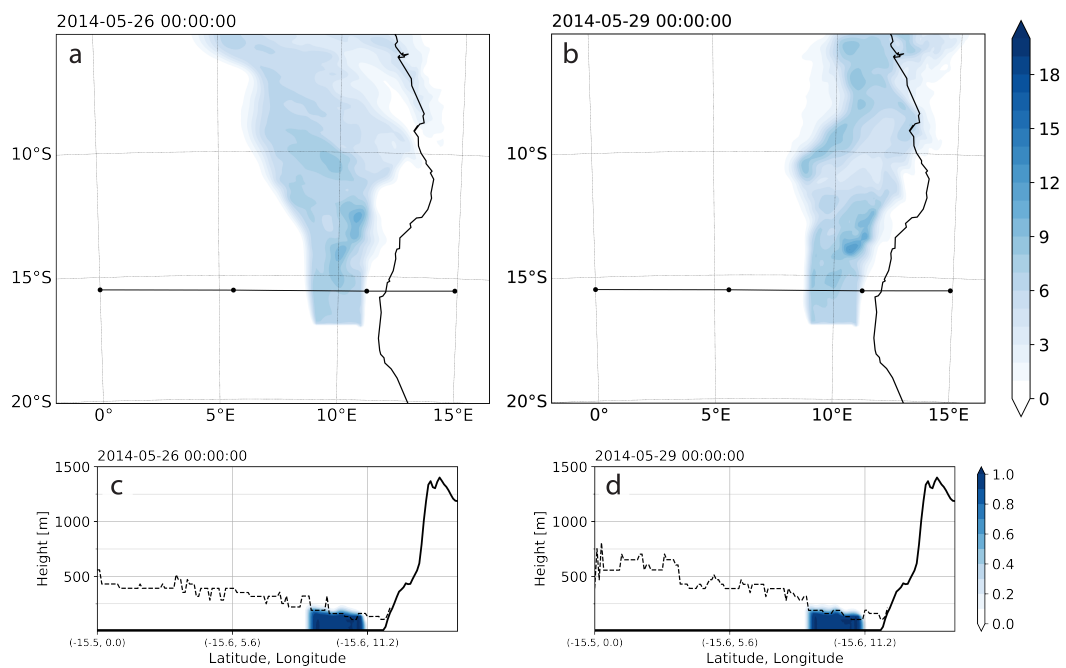


FIG. 9. As in Fig. 8 but for the same two active #2 period times as in Fig. 5.

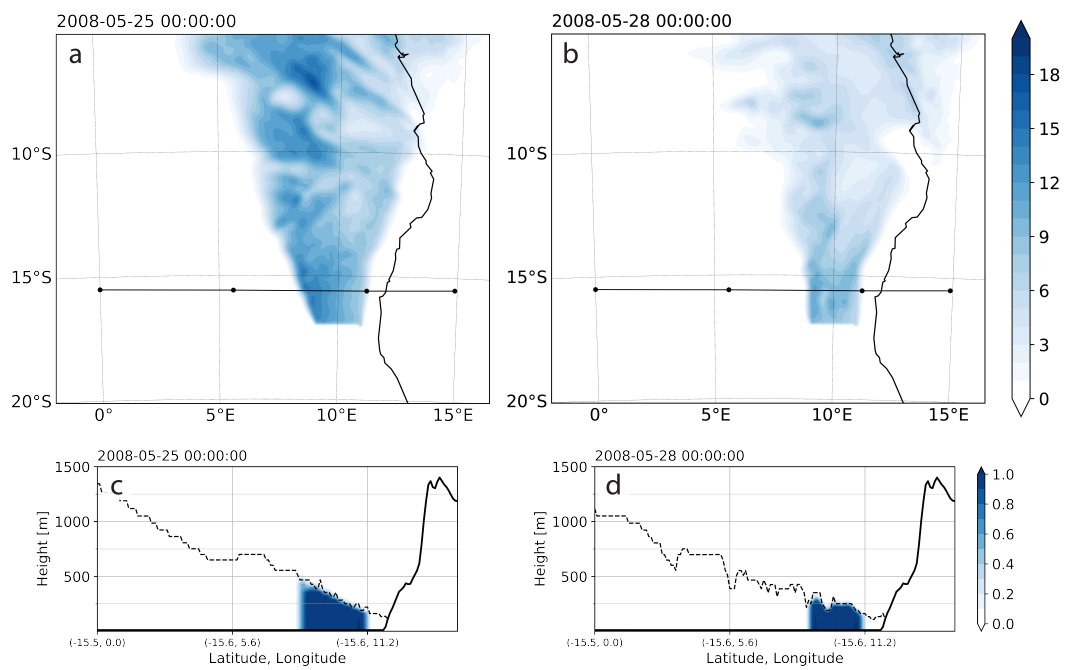


FIG. 10. As in Fig. 8 but for the same two null #1 period times as in Fig. 6.

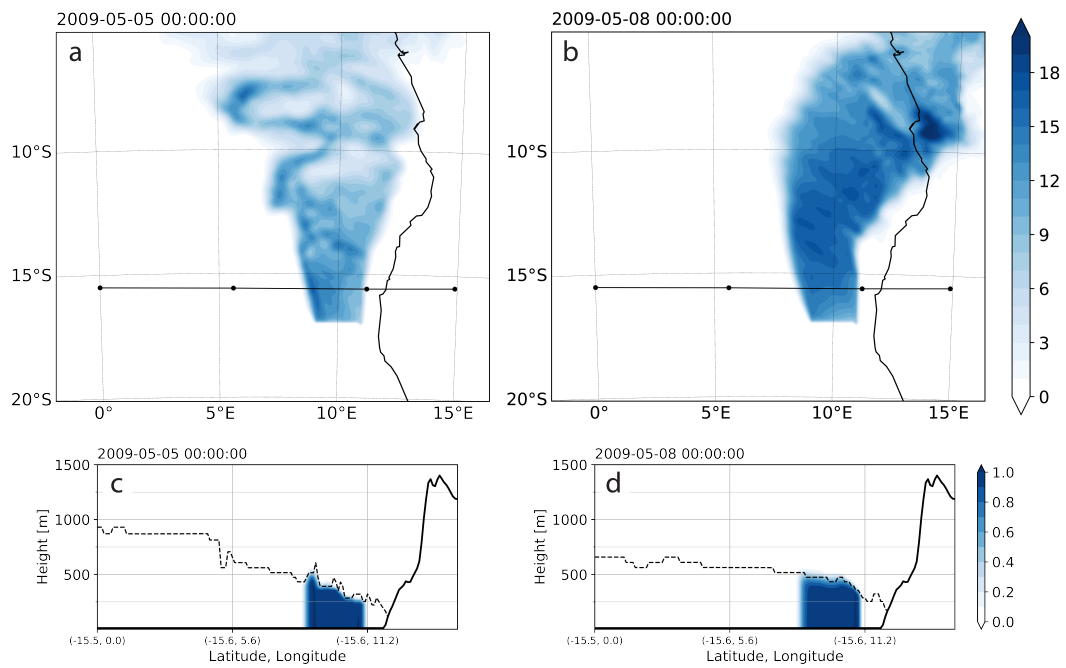
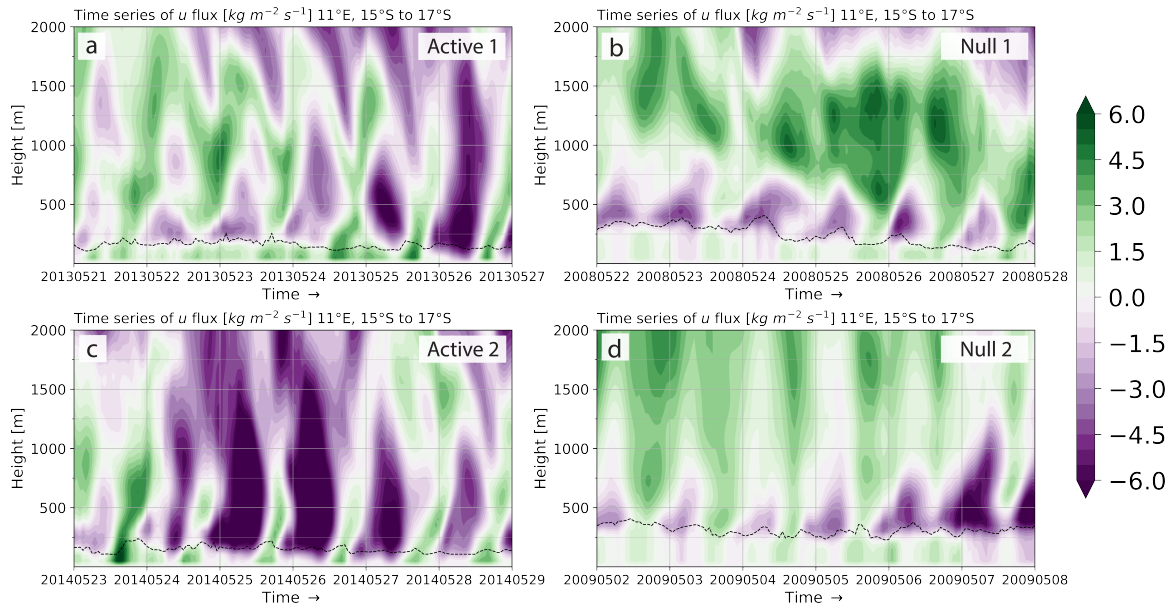


FIG. 11. As in Fig. 8 but for the same two null #2 period times as in Fig. 7.



583 FIG. 12. Time series of mass flux ( $\text{kg m}^{-2} \text{s}^{-1}$ ) from 0 m to 2000 m every 50 m for (a) Active # 1 period, (b)  
 584 Null # 1 period, (c) Active #2 period, and (d) Null #2 period, averaged over the 200-km wide black line in Figure  
 585 1. Dashed black line shows averaged boundary layer height. Purple colors indicate areas where there is offshore  
 586 flow and green colors indicate areas where there is onshore flow.

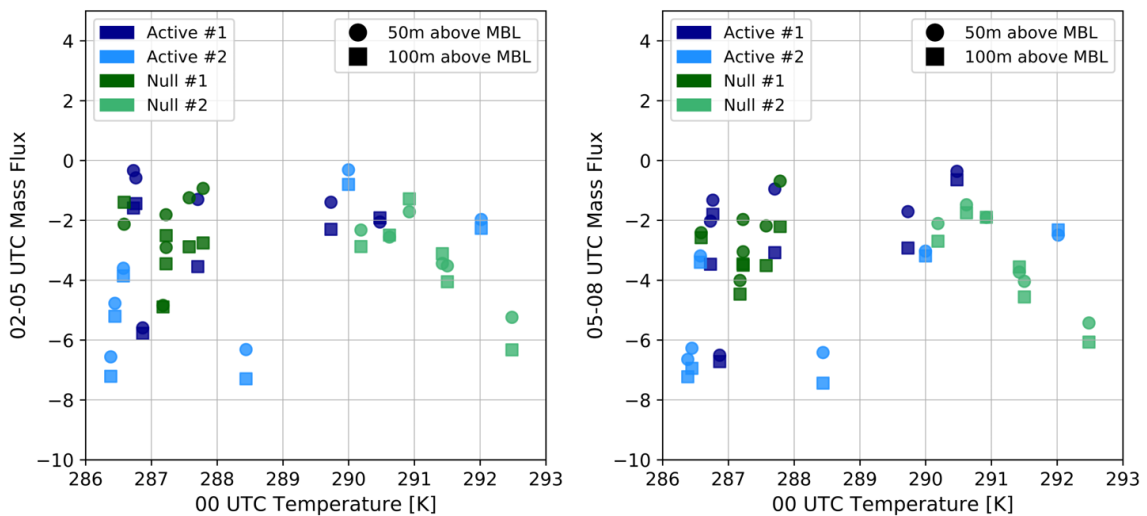


FIG. 13. Scatter plot of 0000 UTC temperature averaged over red box in Figure 1 compared to 0200–0500 UTC (left) and 0500–0800 UTC (left) average mass flux from black line in Figure 1. Points are distinguished for each simulation, Active #1 (dark blue), Active #2 (light blue), Null #1 (dark green), and Null #2 (light green) and for 50 m (circles) and 100 m (squares) above the average boundary layer height.

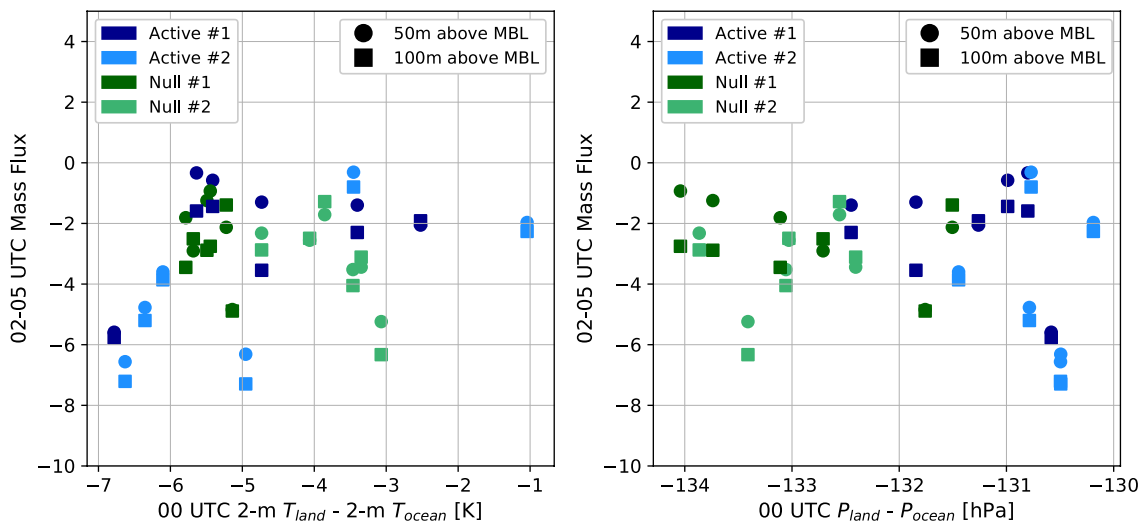


FIG. 14. As in Fig. 13 except for the difference between 2 m temperature over land and ocean (left) and difference between surface pressure over land and ocean compared to the 0200–0500 UTC average mass flux. Ocean values are averaged over 15–20 °S and 5–10 °E.

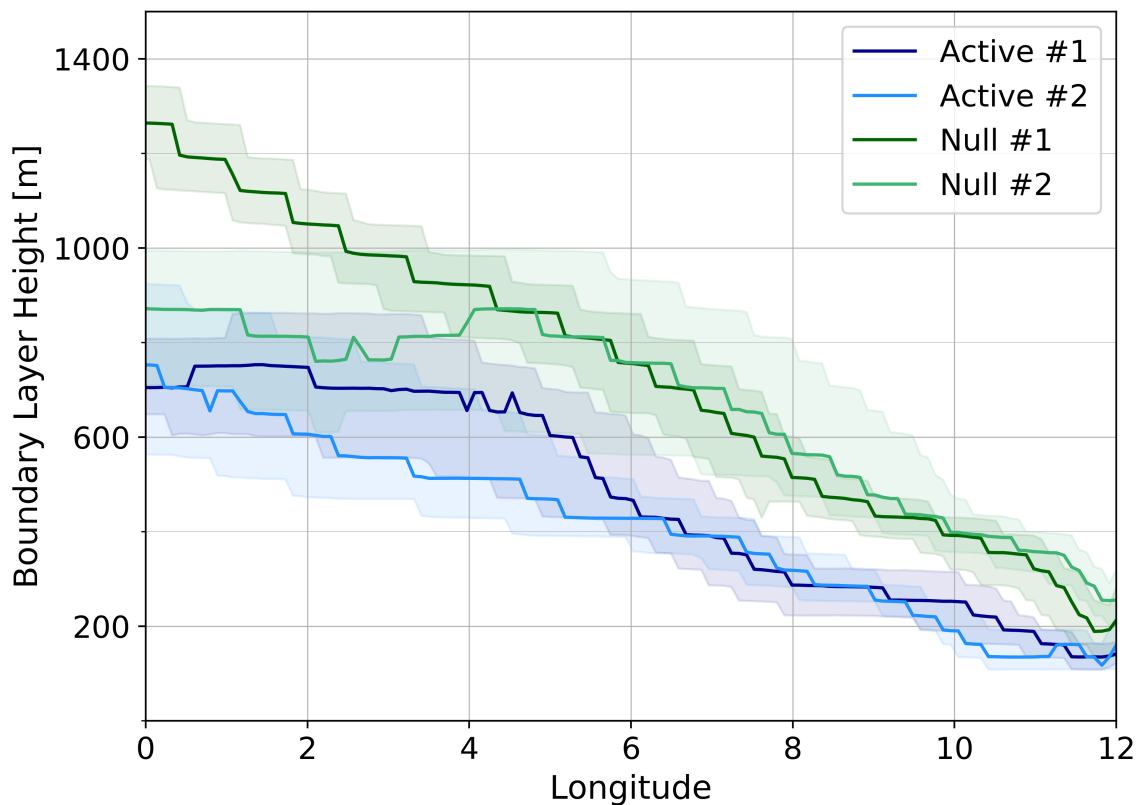


FIG. 15. Calculated median boundary layer height (m) as a function of longitude calculated over a latitude range from 15°S to 20°S for the Active #1 period (dark blue), Active #2 period (light blue), Null #1 period (dark green) and Null #2 period (light green) during the night (0200–0600 UTC). Shaded regions show the interquartile range.

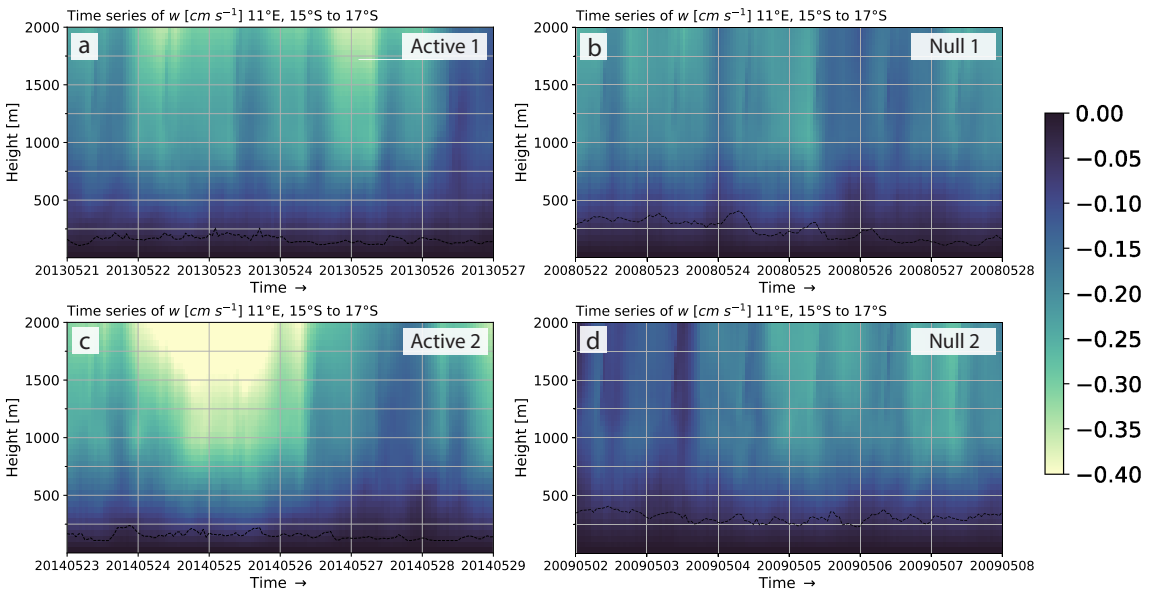


FIG. 16. As in Fig. 12 except for vertical motion ( $\text{cm s}^{-1}$ ). Light green and yellow colors indicate areas of downward motion and dark blue colors indicate areas of upward or negligible motion.

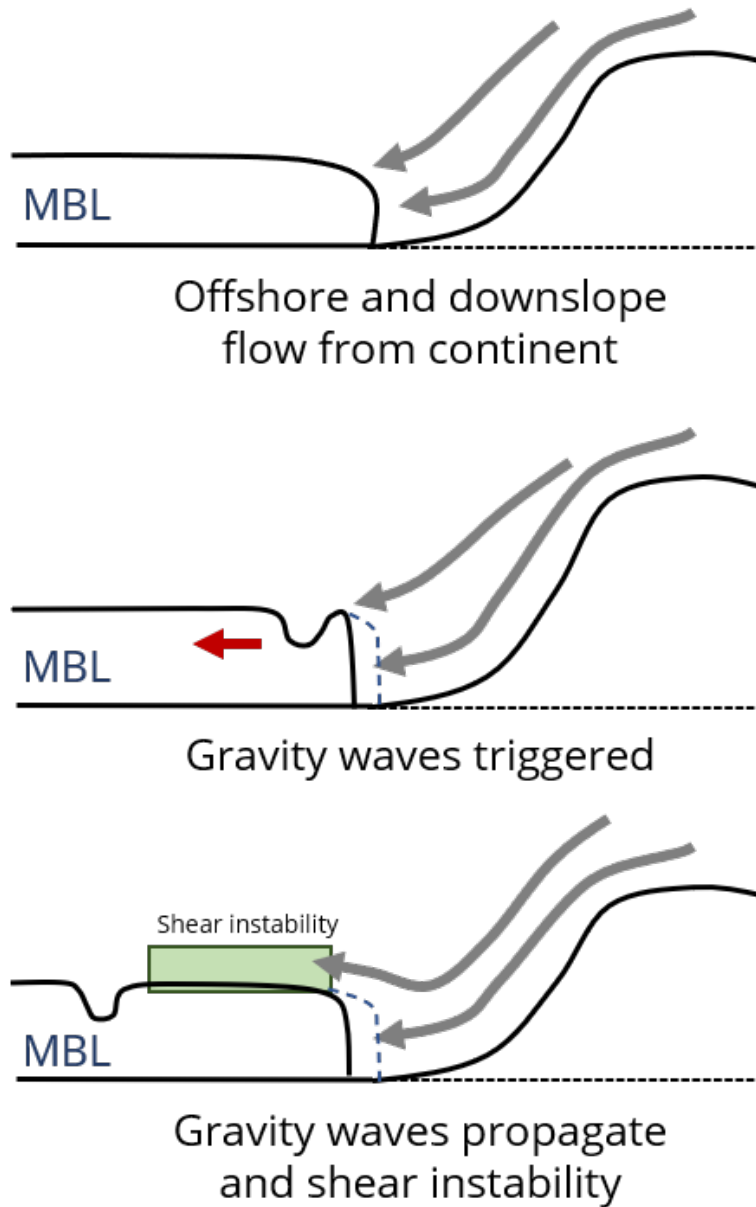


FIG. 17. Conceptual model showing cross sections for 3 sequential times (a–c) during a cloud-eroding event. The cross sections are along a representative latitude (e.g.  $15.5^{\circ}\text{S}$  as in Figs. 4–11) and indicate the relative locations of the MBL top (black line) and land (brown). Gray arrows represent the offshore flow from the continent. Blue dashed line at  $12^{\circ}\text{E}$  in (b) and (c) indicate the original position of the MBL edge in (a). The red arrow in (b) shows the motion of the gravity wave. The green box in (c) indicates a region of shear instability generated by the offshore flow overriding the MBL.